

12-2013

Multiscale contact mechanics model for RF-MEMS switches with quantified uncertainties

Hojin Kim

Purdue University, Birck Nanotechnology Center, kim0@purdue.edu

Nurul Huda Shaik

Purdue University, nurul@purdue.edu

Xin Xu

Purdue University

Arvind Raman

Purdue University, raman@purdue.edu

Alejandro Strachan

Purdue University, Birck Nanotechnology Center, strachan@purdue.edu

Follow this and additional works at: <http://docs.lib.purdue.edu/nanopub>



Part of the [Nanoscience and Nanotechnology Commons](#)

Kim, Hojin; Shaik, Nurul Huda; Xu, Xin; Raman, Arvind; and Strachan, Alejandro, "Multiscale contact mechanics model for RF-MEMS switches with quantified uncertainties" (2013). *Birck and NCN Publications*. Paper 1555.
<http://dx.doi.org/10.1088/0965-0393/21/8/085002>

This document has been made available through Purdue e-Pubs, a service of the Purdue University Libraries. Please contact epubs@purdue.edu for additional information.

Multiscale contact mechanics model for RF–MEMS switches with quantified uncertainties

This content has been downloaded from IOPscience. Please scroll down to see the full text.

2013 Modelling Simul. Mater. Sci. Eng. 21 085002

(<http://iopscience.iop.org/0965-0393/21/8/085002>)

View [the table of contents for this issue](#), or go to the [journal homepage](#) for more

Download details:

IP Address: 128.46.221.8

This content was downloaded on 24/02/2014 at 15:42

Please note that [terms and conditions apply](#).

Multiscale contact mechanics model for RF–MEMS switches with quantified uncertainties

Hojin Kim¹, Nurul Huda Shaik², Xin Xu², Arvind Raman² and Alejandro Strachan¹

¹ School of Materials Engineering and Birck Nanotechnology Center, Purdue University, West Lafayette, Indiana 47907, USA

² School of Mechanical Engineering and Birck Nanotechnology Center, Purdue University, West Lafayette, Indiana 47907, USA

E-mail: strachan@purdue.edu

Received 30 May 2013, in final form 16 September 2013


Published 16 October 2013

Online at stacks.iop.org/MSMSE/21/085002

Abstract

We introduce a multiscale model for contact mechanics between rough surfaces and apply it to characterize the force–displacement relationship for a metal–dielectric contact relevant for radio frequency micro-electromechanical system (MEMS) switches. We propose a mesoscale model to describe the history-dependent force–displacement relationships in terms of the surface roughness, the long-range attractive interaction between the two surfaces, and the repulsive interaction between contacting asperities (including elastic and plastic deformation). The inputs to this model are the experimentally determined surface topography and the Hamaker constant as well as the mechanical response of individual asperities obtained from density functional theory calculations and large-scale molecular dynamics simulations. The model captures non-trivial processes including the hysteresis during loading and unloading due to plastic deformation, yet it is computationally efficient enough to enable extensive uncertainty quantification and sensitivity analysis. We quantify how uncertainties and variability in the input parameters, both experimental and theoretical, affect the force–displacement curves during approach and retraction. In addition, a sensitivity analysis quantifies the relative importance of the various input quantities for the prediction of force–displacement during contact closing and opening. The resulting force–displacement curves with quantified uncertainties can be directly used in device-level simulations of micro-switches and enable the incorporation of atomic and mesoscale phenomena in predictive device-scale simulations.

(Some figures may appear in colour only in the online journal)

 Online supplementary data available from stacks.iop.org/MSMSE/21/085002/mmedia

1. Introduction

Contact mechanics and stiction (static friction) play dominant roles in contacting micro- and nano-systems [1], particle adhesion in microelectronics [2], as well as friction and wear. Contacting micro- and nano-electro-mechanical systems are of interest for capacitive and resistive micro-switches, low-power electronics, and memory devices [3]. Our work is motivated by capacitive radio frequency micro-electromechanical systems (RF-MEMS) switches [4] whose operation involves periodic metal-dielectric contact which are critical for device-operation and can cause device failure. RF-MEMS switch between low and high capacitance states by closing the gap between a metallic membrane and a dielectric landing pad. The device is electrostatically actuated, causing the deflection of the metallic membrane and eventually contact between the metal and the dielectric; removal of the actuation voltage results in the opening of the contact once a threshold value is reached. The force–displacement relationship for the contact upon unloading is particularly important to understand and predict this pull-out or release voltage. While critical for the operation of this and other devices the process of contact unloading after plastic deformation remains poorly understood [5] with significantly less work devoted to it than to purely elastic or reversible contacts.

Significant progress has been made in the understanding of the individual processes that govern contact phenomena at various scales since the initial efforts aimed at capturing the role of roughness in contact mechanics; see, for example, [6, 7]. Recent work led to a fundamental understanding of the molecular and atomic processes [8–12] involved in contact and friction, establishing the limits of applicability of continuum descriptions [13] and characterizing size-dependent plastic deformation [9–11, 14]. Multiscale modeling also contributed to the characterization of thermal transport across rough surfaces [15–17]. At intermediate scales, mesoscale work focused on accurately capturing realistic surface roughness with asperities at multiple scales [6, 18, 19]. Despite this progress little is known about how plastic deformation affects the force–displacement curve, an important phenomena in contacting microsystems. In addition, we are unaware of systematic studies of how uncertainties in the input parameters, those describing the complex surface topographies as well as those associated with materials properties, affect the predictions. Such uncertainty quantification (UQ) studies are critical for the use of force–displacement curves in predictive device-level simulations.

We introduce a multiscale contact model where atomistic simulations and experimental surface topography analysis inform a mesoscale model that predicts the force–displacement curves between two surfaces that can be incorporated in coarse simulations (RF-MEMS device simulations in our case), see figure 1. The mesoscale contact model explicitly describes the rough surface of interest and the evolution of its topography due to localized plastic deformation around asperities when the local stress exceeds the corresponding hardness. The resulting changes in surface topography are permanent; consequently, the model is history-dependent and predicts different loading and unloading force–displacement curves if plastic deformation occurs.

In order to quantify how uncertainties in input parameters affect the predicted force–displacement curves, we first obtain probability distribution functions for all input parameters (experimental and theoretical) that account for uncertainties and intrinsic variability and propagate them through the mesoscale model to characterize how they affect the predicted quantity of interest. As figure 1 shows the input parameters to the mesoscale model have disparate origins and so do the associated uncertainties. The input materials parameters are obtained from extensive atomistic simulations and capture size effects in the plasticity of individual asperities and also account for atomic-level variability and model form errors. Parameters describing the surface topography are obtained from atomic force microscopy

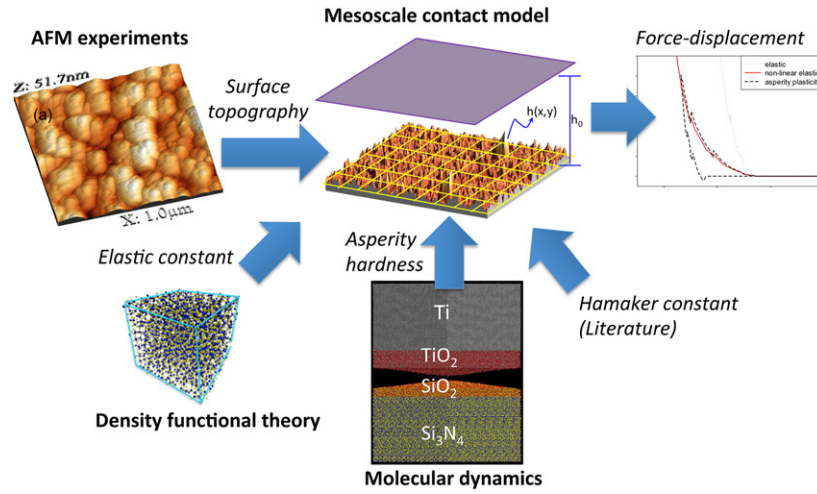


Figure 1. Multiscale model of contact mechanics. The proposed mesoscale contact model captures surface roughness explicitly and predicts force–separation curves; it is informed with experimental surface topography measurements and materials properties from atomistic simulations.

(AFM) experiments and uncertainties are quantified in terms of multiple measurements with various scan resolutions. Finally, the long-range interaction between the surfaces is described via the Hamaker constant corresponding to our surfaces and a range of values is obtained from the literature. An important by-product of the UQ is a sensitivity analysis that provides insight into the dominant processes that govern contact closing and opening.

This paper is organized as follows. In section 2 we introduce the mesoscale contact model and the input information required for predictive simulations. Section 3 describes the characterization of the input materials properties from atomistic simulations including the quantification of the associated uncertainties. Section 4 describes the experimental characterization and the spectral analysis of the surfaces of our devices of interest and how this information is used in the mesoscale contact model. Displacement curves predicted by the multiscale model are shown in section 5. Section 6 describes how uncertainties in the input parameters and the intrinsic variability of the problem at atomic and nanometer scales lead to uncertainties in the force–displacement relationships. Finally, conclusions are drawn on section 7.

2. Mesoscale contact mechanics model

The objective of the mesoscale contact mechanics model is to predict the normal interaction force between rough surfaces as a function of the mean separation distance h_0 in terms of surface roughness and fundamental materials properties of the surfaces involved. In the microsystem of interest, the dielectric surface exhibits considerably more roughness than the metallic one (see section 4); thus, we simulate the interaction between a rough surface and a flat one. This is not a severe limitation since, neglecting transverse sliding, the elastic problem of two contacting rough surfaces is equivalent to a flat surface interacting with a second one with an effective roughness [7].

Consider a rough surface described by the function $h_0 + h(x, y)$, defined so that its mean value is h_0 , that is brought in contact with a flat surface located at $z = 0$; with this definitions the mean separation between surfaces is h_0 , see figure 2.

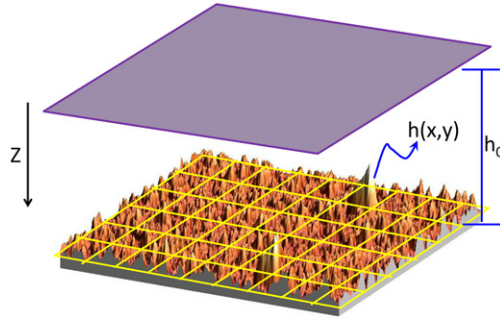


Figure 2. In our setup a rough surface with topography $h_0 + h(x, y)$ interacts with a flat one at $z = 0$.

We compute the force between the two surfaces as the sum of two terms [1]; (i) a long-range attractive interaction that originates in the London dispersion interactions between atoms in the two materials and (ii) a short-range repulsive interaction associated with the solid–solid contact between asperities. While this is a good approximation for a wide range of contacts, it neglects the adhesion due to capillarity that occurs when liquid films are present on the surface [20] and the possible formation of solid bridges between the two surfaces that can occur at high temperatures (for example when an electrical current flows through the contact) [21]. In our model, the surface topography is discretized over a square grid of spacing Δr , the surface topography at each grid point will be denoted as $h(i, j)$, where i and j are integers.

2.1. Attractive interaction term

London dispersion forces between atoms originate from the interaction between induced dipoles and have an inverse sixth power relationship with the interatomic distance [22]. Adding the individual contributions of atoms in two semi-infinite blocks whose surfaces are separated by distance h_0 leads to the Hamaker relationship [23]: $F = -\frac{A_H}{6\pi h_0^3}$ where A_H is the Hamaker constant; a material parameter that depends on the chemistry of the two surfaces. For a rough surface as in our case, the attractive force can be written as a sum over the surface [1]:

$$F^{\text{Ham}} = \sum_{i,j} -A_H \frac{\Delta r^2}{6\pi (h(i, j) + h_0)^3}. \quad (1)$$

Hamaker constants are available for the surfaces of interest and combination rules have been developed for the calculation of pairwise interactions [24].

2.2. Repulsive contact forces

As the two surfaces are brought together asperities will eventually come into contact resulting in a repulsive force. This force originates from the elastic compression of the asperities and its calculation is complicated by the fact that plastic deformation will occur in asperities where the local stress surpasses their corresponding hardness.

We compute the repulsive force as a sum over asperities that are in contact with the flat surface neglecting the elastic interaction between nearby asperities. In general the repulsive contact will depend on the penetration depth, the shape of the asperity and the mechanical properties of the asperity and substrate (both elastic and plastic responses).

We approximate the shape of the contacting asperities as spheroids with an effective radius of curvature to be discussed below and use the Hertz contact model to compute the repulsive force for individual asperities. The next paragraphs discuss the identification and geometrical characterization of the asperities followed by the elasto-plastic model to compute individual forces.

Identification and geometrical characterization of asperities. The contacting surface sites for an average separation h_0 will be given by the grid points for which $h(i, j) + h_0 < 0$. A contacting asperity region is defined as a non-simply connected set of contacting grid points that are separated from other asperities by grid points that are not in contact ($h(i, j) + h_0 > 0$). For each asperity we numerically compute their effective curvature needed for the contact force calculation as

$$R^{-1} = \frac{1}{2\Delta r} \sum_{i,j} \left[\left(\frac{2h(i, j) - h(i-1, j) - h(i+1, j)}{1 + (h(i+1, j) - h(i-1, j))/2} \right)^{\frac{3}{2}} \right] + \frac{1}{2\Delta r} \sum_{i,j} \frac{1}{2} \left[\left(\frac{2h(i, j) - h(i, j-1) - h(i, j+1)}{1 + (h(i, j+1) - h(i, j-1))/2} \right)^{\frac{3}{2}} \right], \quad (2)$$

where the sum runs over the contacting sites of the individual asperity.

Elasto-plastic single asperity contact model. Given an asperity with penetration depth δ_i and effective radius of curvature R_i the repulsive force originating from its elastic compression is

$$F_i^{\text{cont}} = \frac{2}{3} E^* \sqrt{R_i \delta_i^3}, \quad (3)$$

where δ_i and R_i are the indentation depth and the mean asperity radius of curvature, and E^* is the effective elastic modulus of the two surfaces obtained as from the Poisson ratios and Young's moduli of the two surfaces: $[\frac{1-\nu_1^2}{E_1} + \frac{1-\nu_2^2}{E_2}]^{-1}$. A_i is the contact area and $H(A_i)$ is the asperity hardness, that is, the stress above which plastic deformation occurs in the asperities. We explicitly acknowledge the size-dependence of hardness which is known to be important at the nanoscale [11, 14].

The simplest way to incorporate plastic deformation during compression is the use the size-dependent asperity hardness as an upper bound of the contact force:

$$F_i^{\text{cont}} = \begin{cases} \frac{2}{3} E^* \sqrt{R_i \delta_i^3} & \text{if } \frac{2}{3} E^* \sqrt{R_i \delta_i^3} < H(A_i) A_i, \\ H(A_i) A_i & \text{otherwise.} \end{cases} \quad (4)$$

In this model we use the Hertz model as long as the local stress on the contact remains below its associated hardness, above this plastic limit we compute the force as the hardness times the contact area. This approach can be implemented numerically very efficiently and captures the effective *softening* of the contact due to plasticity. However, no permanent change is accounted for and if the release of the two surfaces is simulated (contact opening) the force–displacement curve will be identical to the one during approach (closing) even if plastic deformation occurred. Thus, plastic deformation does not result in hysteresis during unloading; it only leads to a modification of the load–deformation curve; thus we will denote this model *non-linear elastic*.

To improve on this simple model and capture the irreversible processes during plastic deformation our second approach modifies the surface topography to mimic plastic deformation. The approach is graphically depicted in figure 3 where the red represents the

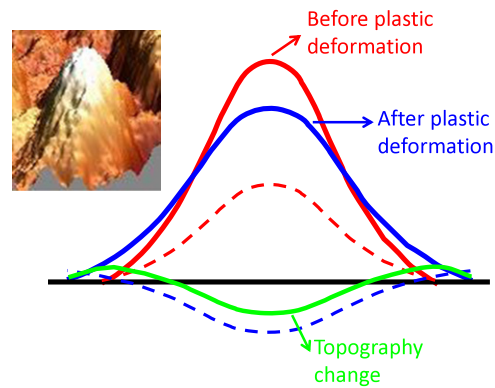


Figure 3. Asperity plasticity model. The surface topography is modified via two Gaussian functions when the local stress is higher than the asperity hardness. A first Gaussian with the curvature of the asperity is used to make the asperity peak flatter, a second, more diffuse Gaussian is used to ensure volume conservation.

surface asperity before plastic deformation and the blue one represents the asperity after plasticity. The change in surface topography should have the following features: (i) It should flatten the top of the asperity. The resulting increase in the contact area A_i and reduction in penetration depth δ_i will bring the stress state closer to the yield surface. (ii) Since plastic deformation is volume-conserving the change in surface topography should have zero mean when integrated in the x - y plane. A simple function to accomplish this is the sum of two Gaussians both centered at the asperity peak, see figure 3. The first Gaussian (dashed red line in figure 3) has the same curvature of the asperity and positive sign so as to flatten the top of the asperity. A second Gaussian is introduced to conserve volume (dashed blue line in figure 3); this function has a radius of curvature three times larger than the one of the first Gaussian, resulting in the surface bulging out around the asperity peak as observed in indentation experiments. The green line in figure 3 denotes the total change in surface topography.

In our implementation of this model we use an iterative procedure with a first (compact) Gaussian with an amplitude of 0.3 nm (the second, diffuse, Gaussian is fully determined by the volume conservation requirement). After each step the average stress on each asperity is computed using the elastic solution in equation (4) and the surface is modified around each of the asperities where the stress surpasses its size-dependent hardness. After the surface topography is modified, the elastic stresses are recomputed with the modified topography and the process is repeated until all asperities are within the elastic limit. This second model will be denoted *asperity plasticity*.

Figure 4 shows the force–displacement curves during closing and opening of the contact of interest using both models. The contact, of nominal area $1\ \mu\text{m} \times 1\ \mu\text{m}$, is closed up to a maximum force of $1 \times 10^4\ \text{nN}$ and then opened. For comparison we include a purely linear-elastic model (dotted line). Both the non-linear and the asperity plasticity models lead to very similar curves during closing. However, while the non-linear elastic model shows the same force–displacement behavior during opening, the asperity plasticity model correctly predicts hysteresis in the force–displacement curve. During contact opening we observe a smaller equilibrium separation between two surfaces and slightly larger attraction due to the flattening of the rough surface.

Our goal of characterizing how the various input parameters affect the predictions of the contact model via uncertainty propagation requires a quantization of the uncertainties in all of

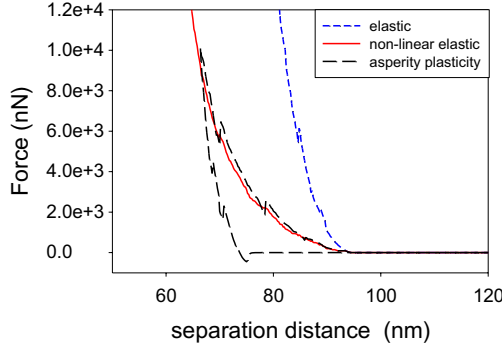


Figure 4. Force–displacement curve for a rough surface comparing the various plasticity models: purely elastic contact (dotted line), non-linear elasticity (dashed) and asperity plasticity (full).

its input parameters. The contact model requires knowledge of the surface roughness which will be obtained via AFM for our surfaces (as described in section 4) and three materials properties: (i) Hamaker’s constant to which our quantities of interest are relatively insensitive to (see section 6) and will be obtained from the literature, (ii) the effective elastic modulus and (iii) size-dependent hardness of the asperities which will be obtained from atomistic simulations in section 3.

3. Informing the mesoscale model with atomistic input

As described in section 2 when two asperities or an asperity and a flat surface come in contact they initially deform elastically but if a critical load, known as asperity hardness, is reached, plastic deformation will occur. Due to the nanoscale nature of the contacts of interest, macroscopic mechanical properties are likely not applicable [9–11, 14]. Thus, we use large-scale molecular dynamics simulations and density functional theory (DFT) to calculate the elastic constants and hardness values required by the mesoscale contact model.

3.1. DFT calculations of elastic constants

The effective elastic constants used in the contact model is a combination of Young’s moduli and Poisson ratio of the two surfaces:

$$E^{*-1} = \frac{1 - \nu_1^2}{E_1} + \frac{1 - \nu_2^2}{E_2}. \quad (5)$$

We ignore the presence of the thin oxide layers in the elastic response. While the elastic constants of crystalline Ti are known with high accuracy [25], amorphous Si_3N_4 can exhibit a range of values due to intrinsic variability and processing conditions. Thus we will combine experimental data for Ti with our own theoretical calculations for the dielectric that include model form and variability associated uncertainties. These calculations are described in detail in [26, 27] and are only briefly described here.

We use DFT to calculate the bulk moduli for an ensemble of Si_3N_4 structures; 138 structures are obtained by annealing molten samples using MD with an empirical potential and fully relaxed (atomic positions and cell parameters) using DFT. We compute the bulk moduli of each of the 138 structures from energy-volume relationships obtained by isotropically

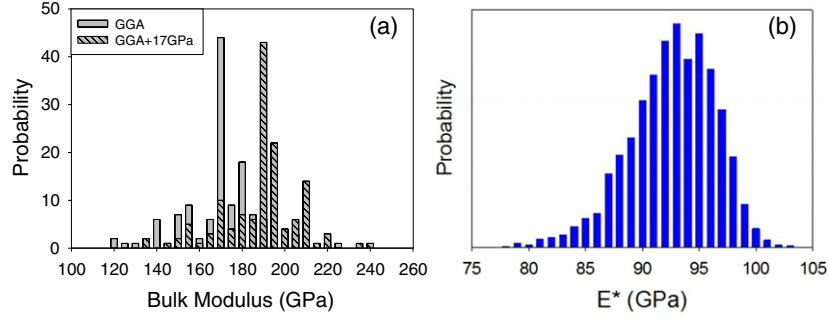


Figure 5. DFT predictions of elastic constant distribution for Si_3N_4 . Both the intrinsic atomic variability of the amorphous network and model form uncertainties are accounted for.

straining samples in a $\pm 5\%$ range, see [26, 27], using the generalized gradient approximation (GGA) to the exchange and correlation functional [28]. The resulting distribution of bulk moduli is shown as full bars in figure 5(a). We obtain Young's moduli from the calculated bulk moduli (B) and the Poisson ratio using the well-known expression for isotropic materials: $E = 3B(1 - 2\nu)$. Experimental values for the Poisson ratio of Si_3N_4 [29] range between 0.15 and 0.25 and we use a uniform distribution between these two values.

The intrinsic variability seen in figure 5(a) are only part of the uncertainty in the elastic constants; the model form error originating from the approximations made in the DFT calculations need to be added. In order to estimate this model form error (that originates in the approximate exchange and correlation functional) we compare the GGA values with local density approximation (LDA) [30], see [27]. We expect the GGA and LDA results to bracket the expected results since GGA is known to often underbind, and LDA tends to overbind. We performed LDA simulations on 108 structures and found that bulk moduli to be, in average, 17 GPa higher than with GGA. Thus, to obtain a distribution of elastic moduli that accounts both for variability and model form error we consider the GGA distribution of bulk moduli and add a second one shifted by 17 GPa to represent the LDA results. The resulting distribution of effective Young's moduli, obtained as a convolution of the DFT bulk moduli distribution and experimental Poisson's ratio, is shown in figure 5(b). The resulting distribution is consistent with range of published experimental values [29].

3.2. Molecular dynamics of asperity hardness

Atomistic model setup. We perform large-scale MD simulations to characterize contact hardness between single asperities in the amorphous Si_3N_4 and Ti surfaces. Both surfaces of the RF-MEMS devices are exposed to air and consequently oxidized; figure 6 shows atomic representations of the surfaces. TEM analysis of the metallic membrane [31] indicates an oxide thickness of approximately 5 nm. The thickness of the SiO_2 oxide layer in the dielectric is estimated to be ~ 2.5 nm based on prior angle-resolved photoelectron spectroscopy experiments [32]. The thickness of the Si_3N_4 and Ti layers in our simulations are 20 nm. To create initial structures for our MD simulations we create films of each material: amorphous Si_3N_4 , SiO_2 , TiO_2 and crystalline (hcp) Ti with the desired thickness and roughness and bring them together. Samples of the amorphous materials are created starting from the melt and annealing them via MD simulations with a cooling rate of 5 K ps^{-1} rate under isobaric, isothermal (NPT) conditions.

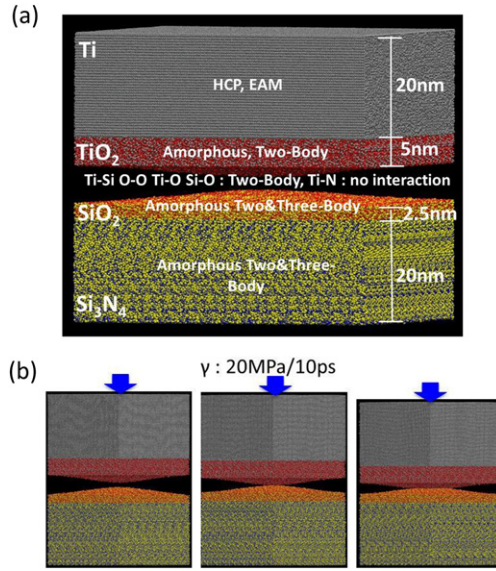


Figure 6. Atomic model for hardness calculations.

As in our previous simulations of metallic contacts [9–11], asperities are created via a sinusoidal surface profile given by

$$Z(x, y) = \min \left[A \sin \left(\frac{2\pi x}{\lambda} \right), A \sin \left(\frac{2\pi y}{\lambda} \right) \right]. \quad (6)$$

We characterized asperity heights A ranging from 1 to 5 nm and peak-to-peak distance λ between 7.2 and 28.8 nm.

Interatomic potential and UQ. Quantifying uncertainties in large-scale MD simulations is challenging due to computational cost of individual simulations and the fact that uncertainties in input parameters are often not known. In our case uncertainties originate from the intrinsic variability of the amorphous systems and from the use of an empirical interatomic potential to describe atomic forces. The intrinsic variability is dealt with by performing a large number of simulations including asperity-asperity and asperity-flat contacts of various asperity heights and peak-to-peak separations. The uncertainties introduced by the force field are *estimated* as described in the following paragraph.

The simulations of interest require modeling of several materials and their interfaces; this is very challenging for force field descriptions which need to capture the various types of bonding and the cross-interactions between materials. The atomistic interactions in all dielectric materials are described by the modified BMK force field [33] for Si_3N_4 , SiO_2 and TiO_2 . All parameters are taken from [33]. Ti metal is described by an embedded atom model potential [34]. Interaction between Ti and N atoms is set to zero since these atom types do not come close to each other during the simulations.

The force field used for the dielectric materials tends to overbind as can be seen by the overestimation in the predicted melting temperature of the bulk materials: $T = 10\,010\text{ K}$ for Si_3N_4 , $T = 6300\text{ K}$ for SiO_2 , and $T = 5100\text{ K}$ for TiO_2 . These values are between 2 and 5 times higher than experiments. Thus, in order to obtain an estimate of the uncertainties

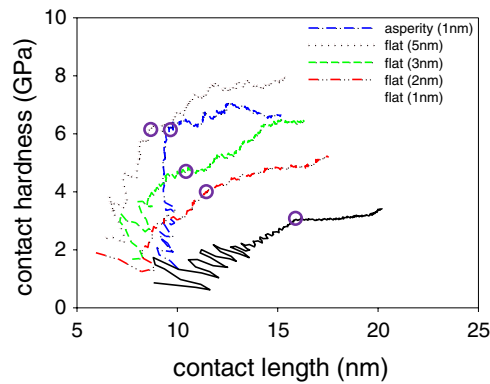


Figure 7. Contact stress as a functional contact area during MD simulations of single asperity contact. Asperity hardness is indicated by a change in slope during loading.

originating from the interatomic potentials used we repeat all simulations with a modified force field obtained by halving all energy terms in the original parameterization. This is admittedly a crude way to estimate uncertainties but it is our best choice due to the computational intensity of the simulations and the lack of other interatomic potentials capable of describing all the interactions required.

Hardness calculations. Asperity/asperity and flat/asperity contacts with various asperity heights are simulated via MD using an approach used previously for metal-metal contacts and described in prior publications [11]; we provide only a brief description here.

Contact simulations are performed via constant-energy MD simulations (NVE ensemble) with an increasing external force applied to both slabs with equal magnitude and opposite direction. This external force (F_{ext}) is applied to all atoms within a thin slab (4.5 nm thick) at the free surfaces away from the contacting ones. The force is increased in steps of $20 \text{ MPa} \times A_{\text{cell}}$ where A_{cell} is the cross-sectional area of the simulation cell. For each level of closing force we perform a 10 ps long simulation. Figure 6(b) shows three atomic snapshots from a representative simulation.

In order to compute the asperity hardness from the MD simulations we need to compute the local stress in the asperities and identify the plastic deformation during loading. In order to obtain the local stress on the contacts we compute the effective contact area (A_{cont}) from each atomistic structure; see [11]. We define contact stress as $\sigma_{\text{cont}} = F_{\text{ext}}/A_{\text{cont}}$ in terms of instantaneous values of force and effective contact area. We monitor local stress at the contact as a function of contact size and identify yield as an abrupt decrease in slope. Figure 7 shows the results of several contact closing simulations. We plot the local stress at the contacts as a function of the contact length (defined as the square root of the contact area) for various cases corresponding to the original force field and a peak-to-peak distance of 28.8 nm. After an initial period of very small contact area, the stress increases as a function of contact length as the contact force is increased. This increase corresponds to the elastic load of the asperities and a change in slope denotes plastic relaxation. The local stress corresponding to this change in slope is defined as the asperity hardness [11, 14] and are marked by circles in figure 7. Perhaps not surprisingly, the results for amorphous contacts presented here show a less drastic plastic relaxation than crystalline metals [11, 14]

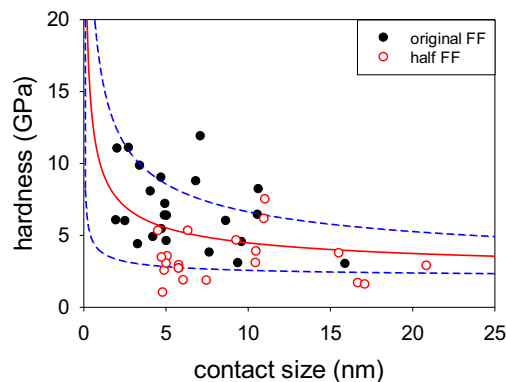


Figure 8. Asperity hardness as a function of contact size from MD simulations. Full symbols show results using the original force fields and open symbols correspond to the force field with halved energies performed to estimate model form uncertainties.

Results: size-dependent hardness. Figure 8 shows the resulting asperity hardness as a function of contact size; filled circle denotes results from the original force field and open circle denotes the force field with halved energies. These values are obtained from multiple MD simulations of contacts with varying asperity curvatures and including asperity/asperity and flat/asperity cases. The results lead to several interesting observations: (i) Asperity hardness increases with decreasing contact size. This trend has been observed in metallic systems [11, 14] and is somewhat surprising and interesting that amorphous systems show the same behavior. The mechanisms responsible for such trends are beyond the scope of this paper. (ii) The intrinsic variability in the atomic structure of the system leads to significant uncertainties in the hardness; interestingly the magnitude of the uncertainty caused by intrinsic variability is comparable to the model form error resulting from the use of the two force fields.

The resulting hardness increase from an average of 10 GPa for contacts of 3 nm in diameter to approximately 2 GPa for 15 nm ones. To extract information that can be used in the mesoscale model we fit our MD data using the function: $H(A) = H_{\text{macro}} + H' A^{-0.25}$ that can be incorporated directly in our mesoscale model, see equation (4). To quantify uncertainties we determine the 68% confidence interval, shown by the dashed lines in figure 8. Thus in the mesoscale simulations the variables H_{macro} and H' are assigned a uniform probability density function in the ranges 0.7–3.2 GPa and 1.95–14.8 GPa nm^{0.5}, respectively.

4. Experimental characterization of the surfaces of interest

The mesoscale contact model requires, in addition to materials properties, a representation of the surface topography. We obtain this information from a spectral analysis of the AFM topography characterization of the surfaces of interest, as described in the next sub-sections.

4.1. Atomic force microscopy

The RF-MEMS switches were carefully flipped using a micromanipulator probe station, allowing both contacting surfaces to be scanned by the AFM. The MFP-3D AFM (AsylumResearch) was operated in the attractive regime of operation wherein the AFM tip makes minimal or no contact with the sample surface and therefore does not affect its roughness. The cantilevers used in our AFM experiments have a typical stiffness of 25 N m⁻¹; and the

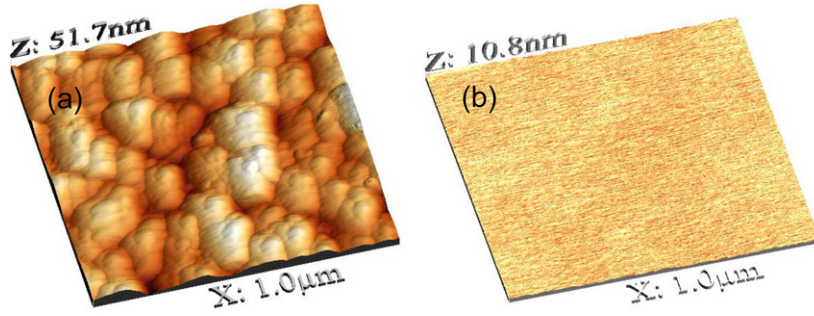


Figure 9. AFM surface topography of the metallic surfaces of the device.

setpoint amplitude is $\sim 90\%$ with the free vibration amplitude of 10–15 nm. All images correspond to 1024×1024 data points, accordingly the resolutions are approximately 1 nm (for $1 \mu\text{m} \times 1 \mu\text{m}$ scans) and 10 nm (for $10 \mu\text{m} \times 10 \mu\text{m}$ scans). Figure 9 shows typical AFM topography images of the Si_3N_4 and Ti surfaces. The Ti surfaces are flatter compared to the Si_3N_4 surfaces. Therefore only the Si_3N_4 surfaces are considered in the spectral analysis and the Ti surfaces are modeled as flat in the contact mechanics simulations.

4.2. Spectral analysis of surface topography

The spectral content of any rough surface can be obtained from its power spectral density (PSD) which can then be used to randomly generate surfaces with the correct statistics [35, 36]. The PSD can be calculated by taking the Fourier transform of the auto-correlation of the height profile [35–38] or computed directly from the Fourier transform of the height profile [35–37]. The latter, more direct, approach is used in this work to calculate the PSD and is briefly described below.

Consider a surface of size $L \times L$, whose height profile z is given by $N \times N$ pixels at grid points (x_m, y_n) , where m and n range from 0, 1, 2, \dots , $N - 1$. Then, its two dimensional discrete Fourier transform is given by

$$Z(q_x, q_y) = \frac{1}{2\pi} \frac{L^2}{N^2} \left[\sum_{n=0}^{N-1} \sum_{m=0}^{N-1} z(x_m, y_n) e^{-j q_x x_m} e^{-j q_y y_n} \right], \quad (7)$$

where $x_m = mL/N$ and $y_n = nL/N$. The spatial sampling frequency will be N/L and the spatial frequencies $f_x = q_x/2\pi$ and $f_y = q_y/2\pi$ range from 0, $1/L$, $2/L$, \dots , $N/2L$. Then, the PSD of the surface can be obtained by squaring the magnitude of its Fourier transform and dividing the result by the area of the surface. Thus we get

$$\text{PSD}(q_x, q_y) = \frac{1}{L^2} \left| \frac{1}{2\pi} \frac{L^2}{N^2} \left[\sum_{n=0}^{N-1} \sum_{m=0}^{N-1} z(x_m, y_n) e^{-j q_x x_m} e^{-j q_y y_n} \right] \right|^2. \quad (8)$$

Note that we assume the topography of our surfaces to be, in average, isotropic. A challenge that arises in the analysis of real surfaces from AFM scans is that we have access to small portions measured on a larger sample. Thus, the height profile is not periodic at the boundaries. This discontinuity or jump at the boundaries results in spurious Fourier components in the spectrum. In order to filter them out, the height profile of the surface is multiplied with a window function which is flat at the center and gradually goes down to

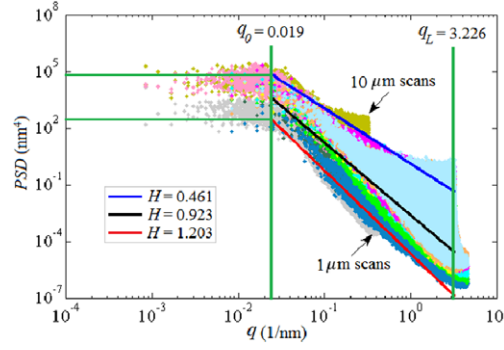


Figure 10. Spectral analysis of the AFM surface topographies.

zero at the boundaries. In the present work, a window that is flat for 99% of the surface at the center is used.

An important step in obtaining a representative spectrum is a quantification of uncertainties and variability. To do this we divide the surface of interest into small portions amenable to AFM scans, analyze each scan and combine the results into a statistical description that captured the observed variability. Each AFM surface scan considered in this work has 1024×1024 pixels and is sub-divided into 100 sections of 768×768 pixels and the results averaged.

We performed this analysis over eight scans of $1 \mu\text{m} \times 1 \mu\text{m}$ surfaces and three of $10 \mu\text{m} \times 10 \mu\text{m}$ ones. The resulting PSD's are plotted as a function of wave vector magnitude $q = \sqrt{q_x^2 + q_y^2}$ in figure 10 in a log-log scale. The results show the expected behavior for rough surfaces [35, 36]: a power-law relationship with an exponent known as Hurst's (H_{exp}) from a cutoff wave vector (q_1) to a roll-off value (q_0); and a plateau for wave vectors below q_0 and down to a minimum value denoted q_L (associated with the size of the scan L by $2\pi/L$):

$$\text{PSD}(q) = \begin{cases} C_0 & \text{if } q_L \leq q \leq q_0, \\ C_0 (q/q_0)^{-(2H_{\text{exp}}+1)} & \text{if } q_0 < q \leq q_1. \end{cases} \quad (9)$$

Figure 10 shows the significant scatter of the data for our surfaces, our goal is to extract parameters with associated uncertainties that can be used in the mesoscale model. In order to obtain q_0 , we fit (least squares) straight lines to the plateau region of the log PSD - log q data between q_L and a variable q such that $q > q_L$. The q value at which the slope of the fitted straight line starts to deviate significantly from zero is taken as q_0 . Similarly, to obtain q_1 we fit a straight line (least squares) to the log PSD - log q data between q_0 and a variable q such that $q > q_0$. The slope of the fitted line, $-(2H_{\text{exp}} + 1)$, is plotted against q . The value of q below which the slope becomes independent of q is taken as the cutoff value q_1 and from that slope, Hurst exponent (H_{exp}) is obtained.

The values obtained for q_0 and q_1 are $\sim 0.02 \text{ nm}^{-1}$ and $\sim 3.23 \text{ nm}^{-1}$ respectively. The H_{exp} value obtained is ~ 0.92 and it corresponds to the slope of the black line in figure 10. In order to quantify uncertainties, the H_{exp} values are obtained (blue and red lines) that bound the scatter in the PSD data between q_0 and q_1 . Thus we obtain a range of H_{exp} between 0.46 and 1.20.

The RMS roughness can be obtained directly from the height profile of the surface [36–38] or from the PSD value in the flat region between q_L and q_0 [35–38]. The two green horizontal lines in figure 10 are the boundaries that determine the minimum and maximum values of RMS roughness. The range of RMS roughness based on the surfaces considered is found to be from

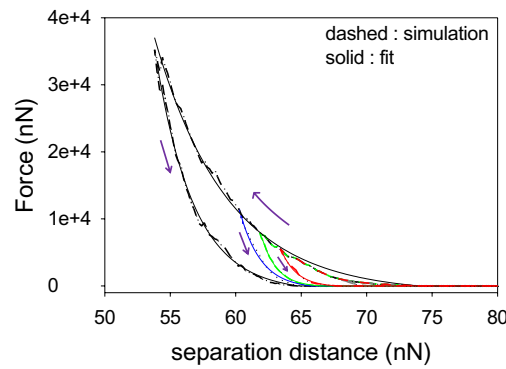


Figure 11. Force–displacement curves up to various maximum loads using mean values for all input parameters.

Table 1. Input Parameters distributions for the mesoscale contact model. Hamaker constant, effective elastic constant, asperity hardness parameters, roll-over wave vector, Hurst exponent and RMS surface roughness.

Parameter (unit)			Source
A (10^{-18} J)	min = 0.18	max = 0.25	Ref [23, 24]
E^* (GPa)	mean = 91	dev = 3.8	DFT
H_{macro} (GPa)	min = 0.7	max = 3.2	Ref [39]
H' (GPa nm $^{0.5}$)	min = 1.95	max = 14.8	MD
q_0 (nm $^{-1}$)	min = 0.015	max = 0.035	AFM
H_{exp}	min = 0.5	max = 1.0	AFM
RMS (nm)	min = 2	max = 15	AFM

~1.82 nm to ~14.17 nm. Based on these values, randomly rough surfaces are generated and are used in simulating the contact mechanics of micro switches.

5. Force–displacement relationships

Figure 11 shows several force–displacement curves predicted by the proposed mesoscale model using atomistic and experimental input parameters; these results are obtained using the mean value for each input parameter; Table 1 summarizes all input parameter distributions. The simulations correspond to maximum contact forces between 5×10^4 to 1×10^3 nN and clearly show the ability of the model to describe the hysteresis during contact loading and unloading.

To quantify the variability of the predictions of the mesoscale contact model due to the uncertainties in its input parameters we need to reduce the output numerical curves into a few parameters that can be quantified. Thus we fit the output force–displacement curves using a function that describes the data accurately. These fits are also critical to use the results of the mesoscale model in device-level simulations.

The total force is described as the sum of an attractive (f_a) and repulsive (f_r) contributions as a function of the mean surface separation h_0 .

$$f_a(h_0) = -A_{\text{cell}} \frac{A}{6\pi d_{\text{shield}}^3(h_0)} - C_a d(h_0 - d_c - \rho_a), \quad (10)$$

where A_{cell} is the cross-sectional area of the simulation cell and A is the Hamaker constant. The first term guarantees a correct description for long separation distances (Hamaker expression for flat surfaces) and the second term corrects the behavior at short distances where nearby asperities experience larger-than-average attraction. The function $d(x)$ measures penetration between the two surfaces and is defined as

$$d(x) = \begin{cases} 0 & \text{if } x > 0, \\ -x & \text{if } x < 0. \end{cases} \quad (11)$$

Parameter d_c is equilibrium contact separation (the average separation between the two surfaces at initial contact) and ρ_a is a characteristic distance for the attractive interaction. Finally, we use a shielded distance to compute the Hamaker interaction to avoid divergences at zero:

$$d_{\text{shield}}(x) = \begin{cases} (x^3 + \alpha^3)^{\frac{1}{3}} & \text{if } x > 0, \\ -\alpha & \text{if } x < 0. \end{cases} \quad (12)$$

The repulsive force is given by

$$f_r(h_0) = A_{\text{cell}} C_r \left[e^{\frac{d(h_0 - d_c)}{\rho_r}} - 1 \right], \quad (13)$$

where ρ_r and C_r are the tunable parameters to describe repulsive interactions.

In summary, the fitting parameters in these equations represent attractive and repulsive pre-factors (C_a and C_r), the average surface separation at contact (d_c) and two characteristic distances ρ_r and ρ_a . The fits are not sensitive to ρ_a and we fix its value to 2 nm.

Thin lines in figure 11 show the fitted curves for the closing and opening results; we can see that the functional form proposed describes the numerical data with high accuracy. Of course, different parameters need to be used to describe contact closing (approach) and opening (retraction) due to the plasticity-induced hysteresis.

6. UQ in force–displacement

To quantify uncertainties in the predicted quantities of interest we propagate the uncertainties in the input parameters, summarized in table 2, through the mesoscale model using the asperity plasticity model to obtain force–displacement curves with parameters described by distribution functions. A brute-force sampling of the input distribution functions would require an enormous computational effort and thus we use a sparse grid technique to create a response function that is subsequently used to propagate uncertainties. The next subsection describes the methodology used and results are discussed subsequently.

6.1. Response surfaces and uncertainty propagation

Propagating uncertainties in the $n = 6$ input variables of the mesoscale model using a brute-force approach, i.e. drawing numbers from the input distributions and performing mesoscale simulations, would be impractical. Thus, we use a polynomial chaos approach using collocation [40]. The quantities of interests (parameters of the force–displacement relationships) are sampled over a sparse grid using a Smolyak algorithm. The quantities of interest at the nodes of the sparse grid are used to obtain a response surface using Legendre polynomials as the basis set. In this paper we compute a 1st order response function for each output quantity which requires $2 \times n + 1$ evaluations of the mesoscale model. This response surface is then evaluated to propagate uncertainties in the input parameters.

Table 2. Predicted parameters for the force–displacement curves during closing and opening.

	d_c^{close} (nm)	C_a^{close} (unit)	C_r^{close} (unit)	ρ_r^{close} (nm)	δd_c (nm)	δC_a (10^{-5} unit)	δC_r (10^{-4} unit)	$\delta \rho_r$ (nm)
mean	31.8	15.1	6.4	3.31	−3.32	5.5	2.76	−0.641
dev	14.2	18.3	4.25	1.51	2.71	9.0	5.1	1.19

Global sensitivity analysis was performed using the elementary effects method developed by Morris [41] and Campolongo and Saltelli [42]. This is a one-at-a-time method that measures the change in output when one input variable is changed while all others are held constant. This is done at multiple points and the results averaged, giving us the sensitivity measure μ^* . In our case, our UQ tool uses sample points chosen from the same sparse grid it used to build the response surface. Because we used only a first order grid, elementary effects are calculated for each variable while all other input variables are held at their medians. Additional details on the process can be found in [43].

6.2. Uncertainty propagation and sensitivity analysis

Table 2 shows the mean values and standard deviations of the various parameters used to describe the force–displacement relationship obtained by propagating the uncertainties in input parameters through the response surface of the contact model. Our approach leads to full distribution of the force–displacement parameters and those are included in the supplementary material (available at stacks.iop.org/MSMSE/21/085002/mmedia). We show values during contact closing, denoted with the *close* superscript, and the change in each individual parameter during opening after a force of 7×10^3 nN over an area of $1 \mu\text{m}^2$ is applied during closing (parameters starting with δ). Reporting and discussing the change in force–displacement parameters caused by plastic deformation is useful to isolate the irreversible phenomena that occurs during closing. Our results show that the main changes from closing to opening are the reduction of the equilibrium contact distance d_c and a stiffening of the force–displacement curves, marked by an increase in C_r and a decrease in ρ_r . The increase in C_a indicates more attraction during contact opening and is due to the increase in effective contact due to plastic deformation.

We note that the resulting distribution functions include uncertainties in all input parameters, both experimental and computational, and include model form error in the input distributions. However, these results do not include model form error for the mesoscale model itself. The comparison of the two plasticity models during contact closing provide a crude estimate of the model form error but its contribution to the uncertainties in force–displacement should be obtained via experimental measurements and it is beyond the scope of this paper.

Tables 3 shows the sensitivity of each output parameter (during closing and their change during opening) with respect to individual input parameters. Remember that the average separation between surfaces (d_c) controls electrostatic force in RF–MEMS and plays a critical role in the prediction of the pull-out or release voltage. RMS surface roughness plays the dominant role in the equilibrium contact separation during contact closing; however, plastic deformation and the roll-over wave vector play important roles in determining the compressive behavior of the contact which dominates the dynamics of the membrane as it bounces on the substrate. More interestingly, the asperity hardness and all surface topography parameters play important roles in determining the change in equilibrium distance due to plasticity; it is this distance that is relevant to understand pull-out.

Table 3. Sensitivity.

	d_c (nm)	C_a (10^{-5} unit)	C_r (10^{-4} unit)	ρ_r (nm)	δd_c (nm)	δC_a (10^{-5} unit)	δC_r (10^{-5} unit)	$\delta \rho_r$ (nm)
A	0.0	3.56	1.5	0.11	0.0	0.1	0.8	0.03
E^*	0.0	7.56	0.15	0.21	1.0	3.1	1.5	0.4
H_{macro}	0.0	37.5	1.1	0.57	3.0	14.8	6.5	0.6
H_{nano}	0.0	48.8	1.3	0.79	2.4	20.45	4.5	0.2
q_0	4.0	121.6	9.6	1.1	1.8	335.9	5.2	3.3
H_{exp}	3.2	45.9	2.8	0.34	3.0	13.9	1.7	0.7
RMS	49.0	36.6	62.7	5.0	7.8	24.5	15.7	2.4

7. Conclusions

In this paper we introduce a multiscale model of contact mechanics motivated by RF-MEMS switches whose operation involve periodic contacts between a metallic and a dielectric surface. A mesoscale contact model describes the surface topography explicitly using spectral analysis data of AFM surface topography and is further informed from atomistic simulations. A salient feature of the model is that plastic deformation around asperities is described by local, permanent modification of the surface topography. Thus the model is history dependent and can capture the change in force–displacement during contact closing (loading) and opening (release). These permanent changes are important in the prediction of pull-out or release voltage in the RF-MEMS device. We propose an analytical expression for the resulting force–displacement curve that accurately captures the numerical results of the model and can be efficiently incorporated into device-level simulations. We note that the plastic flow rule we use ignores creep deformation; thus our results apply for processes with timescales shorter than those associated with creep. The proposed framework to describe plastic deformation of asperities can easily extended to describe creep; this requires a simple modification in the plastic flow rule.

The input parameters to our contact model (or any other model with similar physics) are not known with high accuracy and the uncertainties associated with them have disparate origins (from intrinsic variability to imperfect knowledge of physics). In this paper we quantified these uncertainties in all input parameters and propagated them through the mesoscale contact model. A sensitivity analysis highlights the importance of the surface topography, not just RMS roughness but also its spectral content; furthermore, the plastic deformation of nanoscale asperities is critical to predict force–displacement during unloading.

Our approach leads to force–displacement curves that describe the contacts of interest whose parameters are known as distributions not as deterministic values. Consequently, the uncertainties in the contact model can be propagated through device-level simulations to assess how they affect device performance. Such probabilistic descriptions go beyond predicting mean performance and are an important step towards the ability to use simulations in decision-making in the area of device design.

Acknowledgments

This work was supported by the US Department of Energy's National Nuclear Security Administration under contract Grant No DE-FC52-08NA28617, Center for the Prediction of Reliability, Integrity and Survivability of Microsystems (PRISM).

References

- [1] Delrio F W, de Boer M P, Knapp J A, David Reedy E Jr, Clews P J and Dunn M L 2005 *Nature Mater.* **4** 629
- [2] Kumar G, Smith S, Jaiswal R and Beaudoin S 2008 *J. Adhes. Sci. Technol.* **22** 407
- [3] Choi W Y, Osabe T and Liu T-J K 2008 *IEEE Trans. Electron Devices* **55** 3482
- [4] Peroulis D 2012 *Capacitive MEMS Switches* 1st Edn (Berlin: Springer) at press
- [5] Kadin Y, Kligerman Y and Etsion I 2006 *J. Mech. Phys. Solids* **54** 2652
- [6] Ciavarella M, Delfine V and Demelio G 2006 *J. Mech. Phys. Solids* **54** 2569
- [7] Greenwood J A and Williams J B 1966 *Proc. R. Soc. Lond. Ser. A* **295** 300
- [8] Mo Y, Turner K and Szlufarska I 2009 *Nature* **457** 1116
- [9] Kim H and Strachan A 2010 *Phys. Rev. Lett.* **104** 215504
- [10] Kim H and Strachan A 2011 *Phys. Rev. B* **83** 024108
- [11] Kim H and Strachan A 2012 *Phys. Rev. B* **86** 064101
- [12] Mordehai D, Rabkin E and Srolovitz D 2011 *Phys. Rev. Lett.* **107** 096101
- [13] Luan B and Robbins M O 2005 *Nature* **435** 929
- [14] Ward D K, Farkas D, Lian J, Curtin W A, Wang J, Kim K-S and Qi Y 2009 *Proc. Natl Acad. Sci.* **106** 9580
- [15] Irving D L, Padgett C W and Brenner D W 2009 *Modelling Simul. Mater. Sci. Eng.* **17** 015004
- [16] Crill J W, Ji X, Irving D L, Brenner D W and Padgett C W 2010 *Modelling Simul. Mater. Sci. Eng.* **18** 034001
- [17] Schall J D, Brenner D W and Padgett C W 2005 *Mol. Simul.* **31** 283
- [18] Persson B N J 2007 *Phys. Rev. Lett.* **99** 125502
- [19] Putignano C, Afferrante L, Carbone G and Demelio G 2012 *J. Mech. Phys. Solids* **60** 973
- [20] Hyman D and Mehregany M 1999 *IEEE Trans. Compon. Packag. Technol.* **22** 357
- [21] Samoilov V N, Sivebaek I M and Persson B N J 2004 *J. Chem. Phys.* **121** 9639
- [22] Ashcroft N W and David Mermin N 1976 *Solid State Physics* (Philadelphia, PA: Saunders College)
- [23] Bergstrom L 1997 *Adv. Colloid Interface Sci.* **70** 125
- [24] Eichenlaub S, Chan C and Beaudoin S P 2002 *J. Colloid Interface Sci.* **248** 389
- [25] Bowman K 2004 *Mechanical Behavior of Materials* (New York: Wiley)
- [26] Vedula R P, Anderson N L and Strachan A 2012 *Phys. Rev. B* **85** 205209
- [27] Anderson N L, Vedula R P and Strachan A 2013 in preparation
- [28] Perdew J P, Burke K and Ernzerhof M 1997 *Phys. Rev. Lett.* **78** 1396
- [29] Khan A, Philip J and Hess P 2004 *J. Appl. Phys.* **95** 1667
- [30] Perdew J P and Zunger A 1981 *Phys. Rev. B* **23** 5048
- [31] Cantwell P R, Kim H, Schneider M M, Hsu H-H, Peroulis D, Stach E A and Strachan A 2012 *J. Microelectromech. Syst.* **21** 840
- [32] Hah S R, Burk C B and Fischer T E 1999 *J. Electrochem. Soc.* **146** 1505
- [33] Su X and Garofalini S H 2005 *J. Appl. Phys.* **97** 113526
- [34] Ackland G J 1992 *Phil. Mag. A* **66** 917
- [35] Persson B N J 2006 *Surf. Sci. Rep.* **61** 201
- [36] Persson B N J, Albohr O, Tartaglino U, Volokitin A I and Tosatti E 2005 *J. Phys.: Condens. Matter* **17** R1
- [37] Sidick E 2009 *Proc. SPIE* **7390** 73900L
- [38] Nayak R P 1971 *ASME J. Lubric. Technol.* **93** 398–407
- [39] Sanosh K P, Balakrishnan A, Francis L and Kim T N 2010 *J. Mater. Sci. Technol.* **26** 904
- [40] Xiu D 2009 *Commun. Comput. Phys.* **5** 242
- [41] Morris M D 1991 *Technometrics* **33** 161
- [42] Campolongo F, Cariboni J and Saltelli A 2007 *Environ. Modell. Softw.* **22** 1509
- [43] Hunt M 2013 Prism uncertainty quantification framework, Purdue University (http://memshub.org/site/memosa_docs/puq/ug/sensitivity.html)